coatings

MDPI

Article

Fabrication and Tribological Properties of Diamond-like Carbon Film with Cr Doping by High-Power Impulse Magnetron Sputtering

Shuai Liu [1], Wenjian Zhuang [1], Jicheng Ding [1,2,*], Yuan Liu [1], Weibo Yu [3], Ying Yang [1], Xingguang Liu [1], Jing Yuan [4] and Jun Zheng [1,*]

[1] Key Laboratory of Green Fabrication and Surface Technology of Advanced Metal Materials, Ministry of Education, Anhui University of Technology, Maanshan 243002, China; liushuaiahut@126.com (S.L.); zwj23auot@126.com (W.Z.); liuy202309@nuaa.edu.cn (Y.L.); yangying@ahut.edu.cn (Y.Y.); sdwfcllxg@126.com (X.L.)

[2] China International Science and Technology Cooperation Base on Intelligent Equipment Manufacturing in Special Service Environment, Anhui University of Technology, Maanshan 243002, China

[3] Changzhou Huachuang Aviation Technology Co., Ltd., No. 539 Xiacheng South Road, Wujin District, Changzhou 213161, China; yuweibo1987@126.com

[4] Anhui HERO Electronic Sci & Tec Co., Ltd., No. 129 West Section of Cuihu Fifth Road, Economic and Technological Developent Zone, Tongling 244002, China; hero88001@163.com

* Correspondence: jcdingxinyang@126.com (J.D.); zhengj_ahut@163.com (J.Z.)

Abstract: The present study aims to investigate the advantages of diamond-like carbon (DLC) films in reducing friction and lubrication to address issues such as the low surface hardness, high friction coefficients, and poor wear resistance of titanium alloys. Cr-doped DLC films were deposited by high-power impulse magnetron sputtering (HiPIMS) in an atmosphere of a gas mixture of Ar and C_2H_2. The energy of the deposited particles was controlled by adjusting the target powers, and four sets of film samples with different powers (4 kW, 8 kW, 12 kW, and 16 kW) were fabricated. The results showed that with an increase in target power, the Cr content increased from 3.73 at. % to 22.65 at. %; meanwhile, the microstructure of the film evolved from an amorphous feature to a nanocomposite structure, with carbide embedded in an amorphous carbon matrix. The sp^2-C bond content was also increased in films, suggesting an intensification of the film's graphitization. The hardness of films exhibited a trend of initially increasing and then decreasing, reaching the maximum value at 12 kW. The friction coefficient and wear rate of films showed a reverse trend compared to hardness variation, namely initially decreasing and then increasing. The friction coefficient reached a minimum value of 0.14, and the wear rate was 2.50×10^{-7} $(mm^3)/(N \cdot m)$, at 8 kW. The abrasive wear was the primary wear mechanism for films deposited at a higher target power. Therefore, by adjusting the target power parameter, it is possible to control the content of the metal and sp^2/sp^3 bonds in metal-doped DLC films, thereby regulating the mechanical and tribological properties of the films and providing an effective approach for addressing surface issues in titanium alloys.

Keywords: HiPIMS; DLC films; Cr doping; microstructure; tribological property

Citation: Liu, S.; Zhuang, W.; Ding, J.; Liu, Y.; Yu, W.; Yang, Y.; Liu, X.; Yuan, J.; Zheng, J. Fabrication and Tribological Properties of Diamond-like Carbon Film with Cr Doping by High-Power Impulse Magnetron Sputtering. *Coatings* **2024**, *14*, 916. https://doi.org/10.3390/coatings14070916

Academic Editor: Manuel António Peralta Evaristo

Received: 3 July 2024
Revised: 14 July 2024
Accepted: 15 July 2024
Published: 22 July 2024

1. Introduction

Titanium alloy materials, as lightweight materials with high strength and a strong corrosion resistance, have broad application prospects [1,2]. For example, in the aerospace field, titanium alloys are used for manufacturing the structural components of aircraft, engine parts, etc., due to their high strength and low density, which can reduce the aircraft weight and improve fuel efficiency [3–5]. In the automotive field, titanium alloys can be used to manufacture high-performance automotive components, enhancing the performance and safety of vehicles. In the medical device field, titanium alloys are widely used in

the production of artificial joints, dental implants, etc., due to their excellent biocompatibility and corrosion resistance, reducing the harmful impact on the human body [6]. However, titanium alloys still face challenges regarding their surface hardness and wear resistance, limiting their use in certain applications. To overcome the shortcomings of the low surface hardness and insufficient wear resistance of titanium alloys [7–9], Physical Vapor Deposition (PVD) technology, with its low temperature and environmentally friendly advantages, can be an effective surface modification method. By depositing PVD films on the surface of titanium alloys without affecting their overall excellent performance, a surface modification treatment can impart high hardness, a low friction coefficient, and excellent wear resistance to titanium alloys, effectively addressing their performance deficiencies [10].

Diamond-like carbon (DLC) films, commonly fabricated by the PVD method, are mainly composed of a metastable structure consisting of sp^3 and sp^2 hybrid carbon bonds, exhibiting good mechanical properties and anti-friction and wear characteristics [11,12]; they are widely applied in the aerospace, hydrogen energy, and biomedical fields [13–17]. Regardless of the type of DLC film, the effective control of process parameters and modifications to the film structure can significantly enhance its anti-friction lubrication properties. This approach effectively addresses the issues of low hardness and severe wear on the surface of titanium alloys. However, pure DLC films have significant internal stress, making them prone to delamination from the substrate. Doping films with metal elements can not only reduce residual stress and improve film/substrate adhesion but also enhance their hardness and frictional properties [18]. Moreover, doping DLC films with metal atoms can create a special nanostructure, endowing the film with the exceptional mechanical and tribological properties that pure DLC films lack. Researchers such as Ding et al. [19] have prepared DLC films with different Nb contents using hybrid magnetron sputtering technology, finding that the addition of metal Nb significantly reduces the internal stress of the film. By adjusting the Nb content, the proportion of sp^2/sp^3 bonds in the film can be altered, thereby regulating the film's mechanical properties. Guo et al. [20] used HiPIMS technology to prepare hydrogen-free Al-DLC films using AlC composite targets at different bias voltages. The results showed that the hardness of the film was significantly varied by changing the sp^3-C bond content through bias voltage adjustments. Santiago et al. [21] found that doping DLC films with 3 at. % Cr made it easier to form a carbon-containing layer on the friction contact surface, leading to a superior high-temperature wear performance during the friction process.

There are various PVD methods for preparing DLC films; among them, direct current magnetron sputtering (DCMS) and arc ion plating (AIP) are the most common PVD sputtering technologies. However, due to its low ionization rate during deposition, DCMS technology may lead to poor film–substrate adhesion [22]. AIP technology tends to produce large particles on a surface, resulting in poor surface qualities and tribological properties. Compared to DC magnetron sputtering and arc ion plating, high-power impulse magnetron sputtering (HiPIMS) technology exhibits higher ionization rates due to the application of very high peak power densities for extremely short periods within a single pulse cycle, significantly enhancing the bombardment and etching effects of deposited ions [23,24]. The energy and density of the participating film-forming ions are higher, which results in a higher film–substrate bonding strength and smoother, denser films with fewer defects and large metal particles [25]. Meanwhile, the energy, flux, performance, and incident angle of the bombarding ions also play a significant role in regulating the film's microstructure and mechanical properties during film growth. Kouznetsov et al. [26] also proposed an enhancement of the target atom ionization rates by increasing the target power density, thus improving the comprehensive performance of deposited films.

In this work, DLC films with different Cr contents, obtained by adjusting the target power, were deposited using HiPIMS technology. The effects of power parameters on the doping content, microstructure, and mechanical and tribological properties of the films were investigated in detail. The relationship between the process parameters and film

structure properties was established, achieving a controllable film structure and providing a new method for the surface modification of titanium alloys.

2. Experiment Details

DLC films were deposited using an industrial-scale sputtering system with Q-Plex coating equipment with the scale of 700 mm × 700 mm × 180 mm. The cylindrical Cr target (ϕ 155 mm × 660 mm, 99.99% purity) was powered by an HiPIMS unit. Titanium alloy (TC4) single-sided polished samples (ϕ 32 mm × 3 mm) and single-crystalline Si (100) wafers were used as experimental substrates. To further remove some contamination on the substrate, prior to deposition, the substrates underwent ultrasonic cleaning in acetone and alcohol for 30 min. Initially, a Cr/CrN transition layer was deposited, followed by the deposition of the Cr-DLC layer. The purpose of the transition layer is to enhance the adhesion between the film and the substrate. The DLC layer deposition temperature was 180 °C, with a substrate bias voltage of −100 V, maintaining a deposition pressure of 0.5 Pa and a deposition time of 90 min. The films were prepared under uniform conditions with an Ar/C_2H_2 ratio of 1:2, and the HiPIMS power frequency was fixed at 4000 Hz. The film structure was adjusted by varying the target power from 4 kW to 16 kW. The specific deposition process parameters for the DLC layer and the transition layer are shown in Table 1.

Table 1. Deposition parameters of Cr-DLC films.

Parameters	Cr	CrN	Cr-DLC
Base pressure (Pa)	5.0×10^{-5}	5.0×10^{-5}	5.0×10^{-5}
Working pressure (Pa)	0.5	0.5	0.5
Bias voltage (V)	−50	−50	−100
HiPIMS power (kW)	15	15	4, 8, 12, 16
Pulse length (μs)	100	100	70
Flow rate (sccm)	Ar: 300	Ar/N_2: 200/100	Ar/C_2H_2: 150/300
Deposition time (min)	15	60	90

A field emission scanning electron microscope (FE-SEM, FEI Nano430, Amsterdam, The Netherlands) was used to observe the surface and cross-sectional morphologies of films, measuring thickness and calculating the deposition rate of films. The X-ray energy-dispersive spectrometer (EDS) attached to the FE-SEM was used to measure the elemental content in Cr-DLC films. A surface profilometer was used to detect film surface roughness (Sa), with a measurement range of 500 μm × 500 μm. A Raman spectrometer was used to analyze the film bonding characteristics. For Raman testing, a wavelength of 532 nm was selected, with wavenumbers ranging from 800 to 2200 cm^{-1} and a minimum spot diameter of 1 μm.

The chemical bonding state was determined using X-ray photoelectron spectroscopy (XPS, Escalab 250Xi, Waltham, MA, USA) using mono Al Kα (hv = 1486.6 eV) at 15 kV and 15 mA. Prior to XPS signal acquisition, the surfaces of films were cleaned with Ar^+ for 120 s. The C 1s binding energy of 284.88 ± 0.14 eV was used for the calibration. The hardness (*H*) and elastic modulus (*E*) of films were tested using a nanoindenter. To ensure reliable testing results were obtained, measurements were taken at ten areas on the film surface, and the average value was recorded. The wear performance of films was evaluated using a ball on disk tribometer. The test conditions included a 9Cr18 steel ball with a diameter of 6.35 mm, a load of 5 N, a linear velocity of 30 cm/s, a rotation radius of 5 mm, and a relative humidity of 40%~60%. After the wearing test, the films were observed using a step profiler and an optical microscopy. Finally, the wear rate (W) was calculated based on the Archard equation:

$$W = V/(N \times L)$$

where V is volume loss, N is the normal load, and L is the total sliding distance.

3. Results and Discussion

The composition of Cr-DLC films prepared at different powers is illustrated in Figure 1. It can be observed that, as the target power increases from 4 kW to 16 kW, the Cr content rises from 3.73 at. % to 22.65 at. %, while the C content exhibits the opposite trend, decreasing from 94.28 at. % to 75.44 at. %. As the target power increases, the HiPIMS peak power density also rises, enabling secondary electrons on the target surface to acquire higher energy and speed. This increases the probability of collisions with the target material, thereby enhancing the Cr ionization rate [27]. Throughout the whole deposition process, the deposition state remains stable, with no apparent arcing on the target surface. This is a significant advantage of the HiPIMS power source, effectively suppressing/delaying arcing compared to traditional DC power sources. Therefore, by adjusting the target power, it is possible to control the Cr doping content to range from trace amounts to high levels. Additionally, an O content below 5 at. % was detected in all films; this could be ascribed to the residual air in the vacuum chamber. The relationship between the film thickness and deposition rate of the films with power variations is shown in Figure 2. As the power increases, the film thickness grows from 1.40 μm to 2.06 μm, and the corresponding deposition rate rises from 15.56 nm/min to 22.90 nm/min. This is due to the increased power leading to higher ion sputtering rates on the target material [28], thereby increasing the probability of collisions with C_2H_2 molecules and subsequently improving the deposition rate of the film. Further increases in power do not significantly alter the deposition rate. Although an excessive target power can improve the ionization rate, increasing the negative potential of the target will attract the ionized target ions back to the target material, which is the self-sputtering effect [29], meaning that there is little change in the deposition rate after the power increases beyond 12 kW.

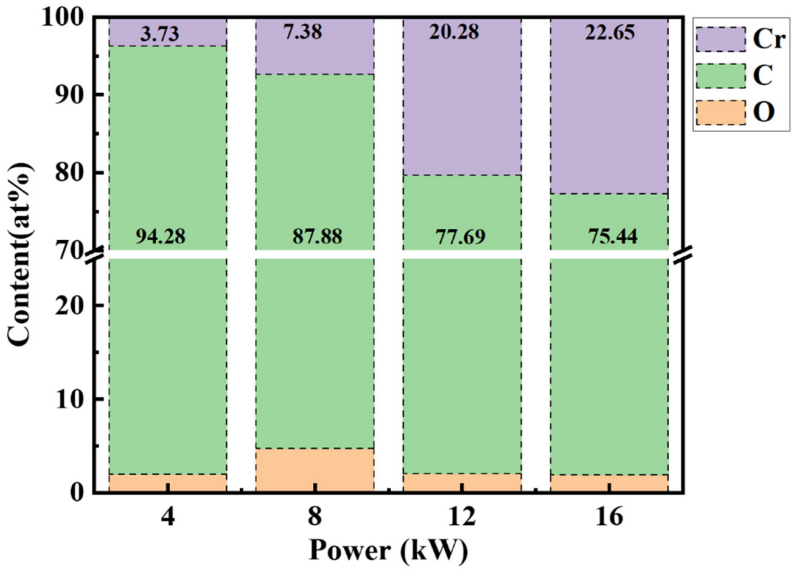

Figure 1. The chemical composition of the films as a function of power.

The surface and cross-sectional morphologies of the films with various target powers were characterized using SEM, as shown in Figures 3 and 4. At 4 kW, the film surface appears smooth and dense, with no significant defects except some particles. As for 8 kW, spherical precipitates are visible on the film surface and these small precipitates are uniformly distributed. At 12 kW, a notable change in morphology occurs, with a transition from cluster formations to fine scale-like structures. At the same time, the film's surface becomes denser, the solid solubility of Cr in the film reaches its limit, and the Cr-rich phase begins to precipitate on the surface. Upon reaching 16 kW, the scale-like structures merge into larger tissues, and the Cr content in the film also reaches the maximum. The corresponding cross-sectional morphologies of films are depicted in Figure 4, showing the films have a uniform growth distribution at all powers and good adhesion with the

substrate interface. The transition layer and DLC layer exhibit an obvious layered structure. As seen in Figure 4a–d, a prominent columnar crystal growth is observed in the transition layer, which is adherent with the DLC layers. With the increase in target power, the thickness of DLC layer increases and the structure shows no obvious changes. The three-dimensional surface morphologies of films with different target powers are shown in Figure 5. As the target power increases, the surface roughness (Sa) of the film decreases from 312.0 nm at 4 kW to 48.3 nm at 8 kW, followed by a slight increase, but stabilizes thereafter. This is attributed to the lower ion energy at lower target powers, which affects the Cr atoms that are uniformly doped in films, leading to an uneven film growth and increasing the probability of the formation of large particles [30]. At a relatively high target power, Cr atoms can achieve sufficient energy for diffusion and migration on the surface of the film, resulting in a smoother and denser film surface. However, with further increases in the target powers, the Cr content in films reaches its solid solution limit, and thus the precipitation of the Cr-rich phases increases the surface roughness. When the number of precipitates increases and they aggregate together, the surface roughness is reduced. Consequently, the Sa value decreases from 147.4 nm at 12 kW to 84.9 nm at 16 kW.

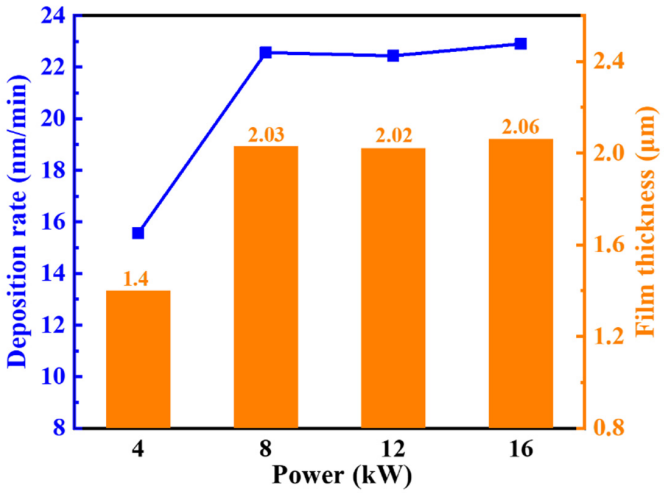

Figure 2. Deposition rate and thickness of the films under different target powers.

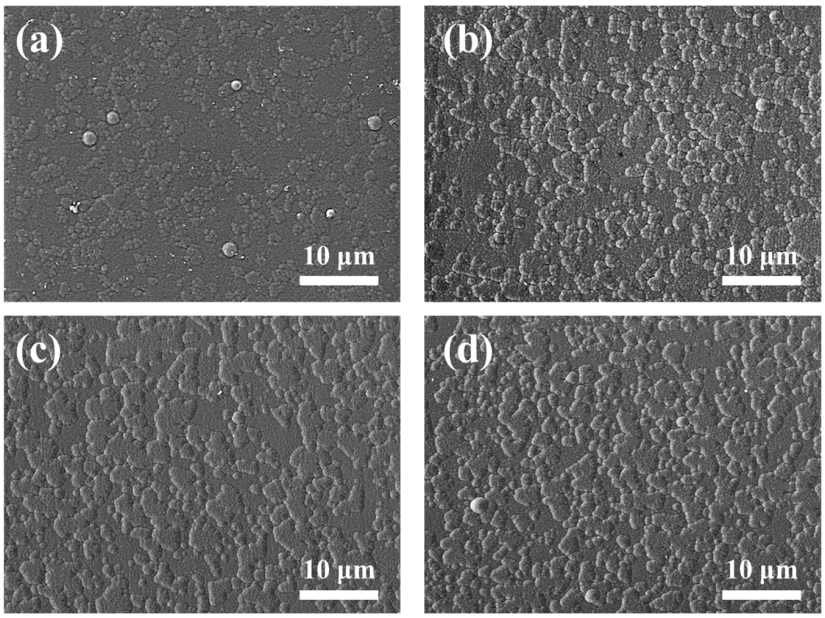

Figure 3. Surface images of films with various target powers: (**a**) 4 kW; (**b**) 8 kW; (**c**) 12 kW; and (**d**) 16 kW.

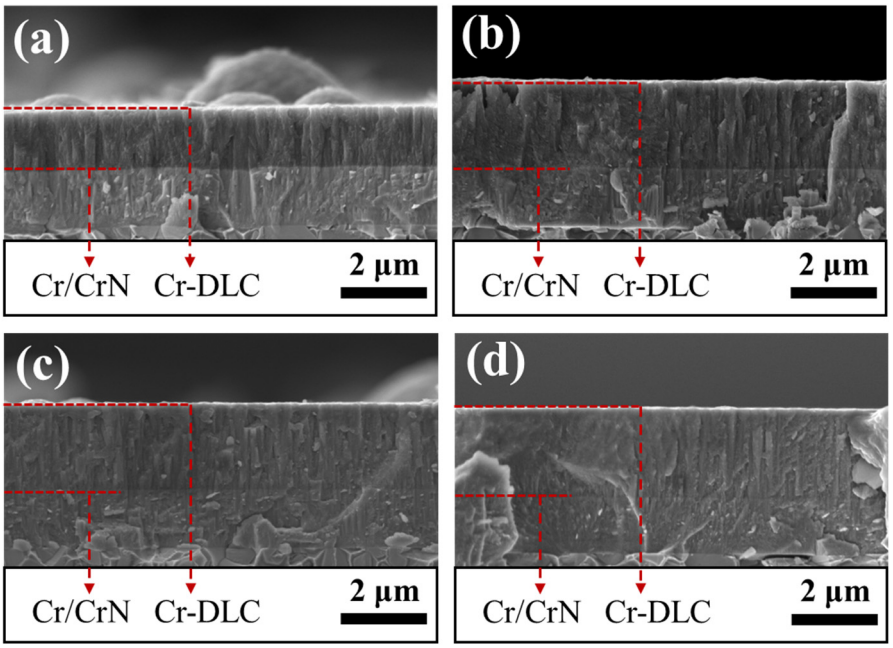

Figure 4. Cross-sectional images of films with various target powers: (**a**) 4 kW; (**b**) 8 kW; (**c**) 12 kW; and (**d**) 16 kW.

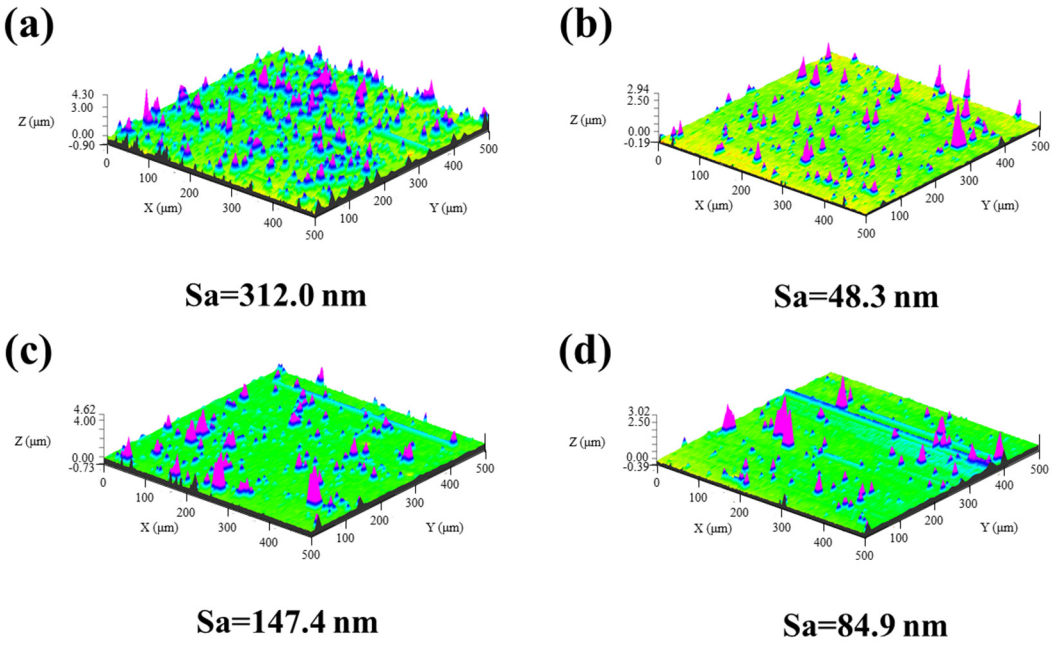

Figure 5. Surface roughness of films with different target powers: (**a**) 4 kW; (**b**) 8 kW; (**c**) 12 kW; and (**d**) 16 kW.

The Raman spectra of films with different target powers are shown in Figure 6. As the power increases, the Raman spectrum signal intensity gradually diminishes, with smaller and weaker peaks. This effect was also observed in previous studies when doping DLC with other metals, such as V and Zr [21,31]. This can be ascribed to the reduction in the light absorption capability of the DLC films when introducing metal dopants. Meanwhile, the intensity of the decrease in the Raman spectra also suggests that the C content decreased in films, which is consistent with the results of Figure 1. The common feature among the four film groups is the appearance of an asymmetric broad peak in the range of 1000–1800 cm^{-1}, with a minor shoulder peak in the low-wave-number region, typical of amorphous DLC film Raman spectra. To further analyze the amorphous carbon bonding

structure in the films, Gaussian fitting was employed to fit the Raman spectra into two Gaussian peaks: the D−peak at around 1360 cm^{-1} due to the breathing vibration of sp^2 atoms, which occurs only in rings, and the G−peak at around 1580 cm^{-1} due to the vibrations of sp^2 atoms in both rings and chains, as shown in Figure 6b,c. A high degree of overlap between the fitting curve and the Raman spectrum curve was obtained, indicating accurate and reliable fitting results. With an increase in target power, the Cr doping level rises, leading to a larger D peak area relative to the G peak area. This signifies an increase in the sp^2/sp^3 bond ratio [32]. This is due to Cr doping promoting an increase in the sp^2−C bond content and the degree of graphitization. Figure 6d presents the I_D/I_G ratios with respect to the target power, where the I_D/I_G increases from 0.50 to 0.93. This indicates a trend of an increase in the content of the sp^2−C bond with an increase in power. The higher Cr doping enhances the film's disorderliness. Moreover, increasing the power enhances the frequency of sputtering particle bombardment on the substrate surface, increasing the film surface temperature and promoting the transition of metastable sp^3−C bonds to sp^2−C bonds.

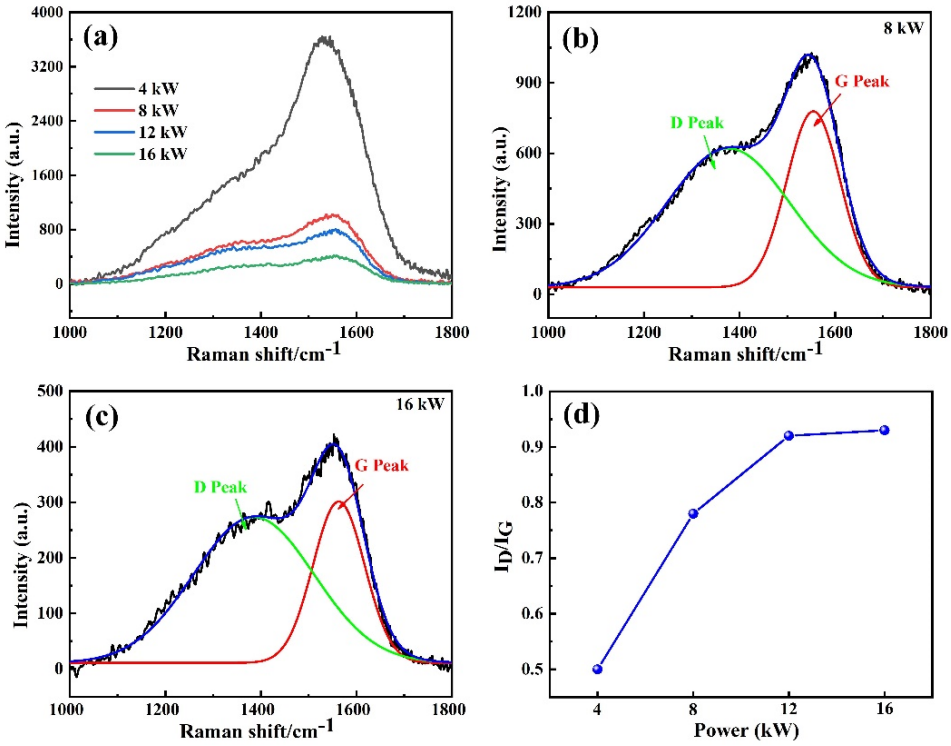

Figure 6. Representative Raman spectra of films under different target powers: (**a**) full Raman spectra, (**b**) 8 kW Raman spectrum, (**c**) 16 kW Raman spectrum, and (**d**) the corresponding I_D/I_G ratio.

To investigate the influence of target power on the chemical bonding status of carbon atoms in the films, C1s' high-resolution fitting analyses were conducted for several film groups, as shown in Figure 7. All films exhibit a main peak at around 284.6 eV and the shoulder peaks at around 283.5 eV can be observed in films deposited at 8, 12, and 16 kW. Especially, the film deposited at 16 kW shows that the intensity of the shoulder peak is comparable to that of the main peak. The C1s peak could be deconvoluted into four peaks at around 287.4 eV, 285.6 eV, 284.7 eV, and 283.1 eV, corresponding to C−O, sp^3−C, sp^2−C, and Cr−C bonds, respectively. The absence of a Cr−C peak in the film deposited at 4 kW is due to the low Cr content, as it primarily exists in a dispersed solid solution form within the amorphous carbon network. Additionally, in Figure 7d, the film displays a low binding energy peak at 282.8 eV, which was attributed to the Cr−C bond. According to previous works, the Cr−C bonds at the binding energy peaks of 282.8 eV and 283.1 eV belong to Cr_7C_3 and Cr_2C_3, respectively [21,33]. As the target power increases, the intensity of the

Cr_2C_3 peaks gradually rises, indicating that the Cr content increases in films. At the highest Cr content, as shown in Figure 7d, the Cr_7C_3 phase appears. As a carbide-forming element, the Cr doped into the film forms carbides with C. Following an increase in Cr content due to the higher Cr target power, the formation of carbides also increases. The presence of C−O bonds may be attributed to the oxygen adsorption on the sample surface in ambient air before XPS detection.

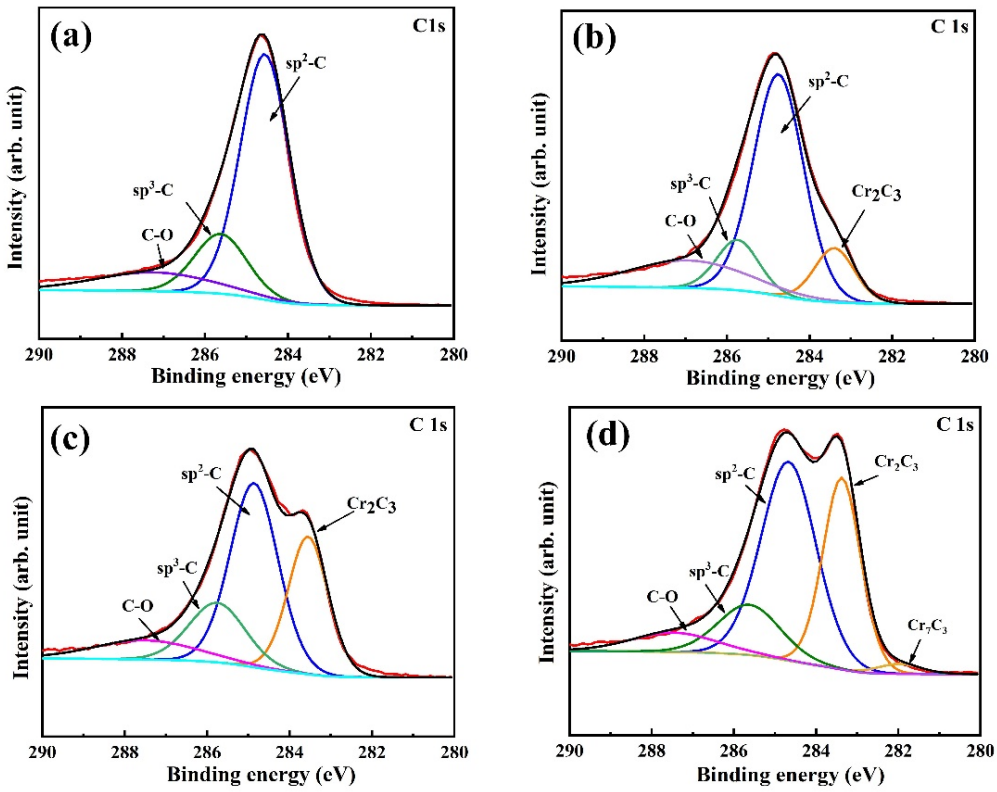

Figure 7. Typical C1s high-resolution XPS spectra of films with various target powers: (**a**) 4 kW, (**b**) 8 kW, (**c**) 12 kW, and (**d**) 16 kW.

The hardness and elastic modulus of films deposited with different powers are shown in Figure 8a. With an increase in power, the film's hardness and elastic modulus exhibit a trend of an initial increase followed by a decrease, reaching the maximum values at 12 kW, measuring at 11.44 GPa and 137.25 GPa, respectively. This is because, in cases with a small amount of doping, the metal Cr is embedded in the three-dimensional network film with different sizes of atomic clusters, which improves the hardness of the film and maintains the toughness of the film. When the Cr doping content is excessive, the strong plasticity becomes dominant, and the hardness and elastic modulus of the film decrease significantly [34]. Throughout the doping process, the elastic modulus and hardness of films demonstrate a trend of an initial increase followed by a decrease. In addition, increasing the power enhances the Cr ionization rate, elevating the Cr content in the film, and the formation of carbides reinforces the film hardness. The surface roughness (Sa) of the film exhibited a decreasing trend, corresponding to the denser structure. This also contributed to the hardness enhancement. With further increases in power, the Cr content stabilizes, but the film's surface temperature rises due to ion bombardment. This leads to graphitization, an increase in sp^2−C bonds, and a slight decrease in film hardness [35]. The characteristic coefficient H^3/E^2, representing the resistance to plastic deformation of the film, decreases with increasing power, as shown in Figure 8b. Typically, a lower H^3/E^2 value indicates a poorer wear resistance of the film [36]. At 4 kw, the plastic factor value is the highest, indicating better resistance to plastic deformation, while at a 16 kW deposition power, the plastic factor value is lowest, indicating poorer resistance to plastic deformation.

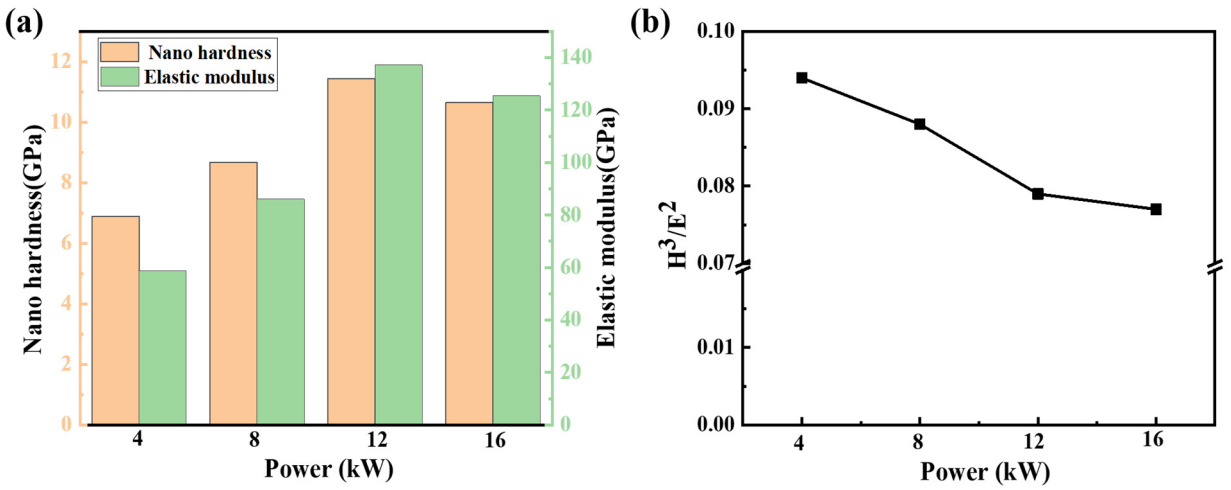

Figure 8. Mechanical properties of films at different target powers: (**a**) hardness and elastic modulus; (**b**) the ratio of H^3/E^2.

The variation in the friction coefficient of films under different target powers is depicted in Figure 9a. The films deposited at relatively low target powers (4 kW and 8 kW) enter a stable friction coefficient (COF) stage after a brief running-in period. At the stable stage, the film deposited at 4 kW showed a COF at around 0.17 and that of the film deposited at 8 kW remained around 0.14. The COFs of the films deposited at high target powers exhibit significant fluctuations, with higher values at the onset of friction. The COF of the film deposited at 16 kW reached 0.5. This is because when the ball and film first come into contact, the ball surface does not form a lubricating transfer film, resulting in higher friction coefficient values within the initial 10,000 cycles. As the number of friction cycles increases, the films gradually enter a stable running-in period, and after 15,000 cycles, the friction coefficients stabilize at around 0.25 and 0.31, respectively. The corresponding wear rates of films are shown in Figure 9c. As the power increases from 4 kW to 16 kW, the wear rate of the film rises from 1.28×10^{-7} $mm^3/N{\cdot}m$ to 2.48×10^{-6} $mm^3/N{\cdot}m$. This is attributed to the presence of hard carbide phases in the film at high doping levels, which cause abrasive wear and result in greater wear depths, leading to an increase in the wear rate [37]. The changing trend of wear rate described above is also consistent with the result of H^3/E^2, shown in Figure 8b.

Figure 10 displays the 2D profile curves of films after the wearing test. At 4 kW power, the film exhibits the shallowest wear scar, less than 0.4 μm deep, and the wear width is around 220 μm. The corresponding wear rate is the lowest, as shown in Figure 9c, indicating superior wear resistance. As the target power increases from 8 kW to 16 kW, the width of the wear scar increases from 188 μm to 430 μm, and the depth increases from 0.5 μm to 2 μm. This is attributed to the higher Cr content resulting in the formation of a large quantity of hard carbides, which act as wear debris, leading to an increase in the friction coefficient. To investigate the reasons for the different performance of films prepared at different powers under the same friction experiment conditions, the wear scars were analyzed using Raman spectroscopy after the friction experiment. The results, as shown in Figure 11, indicate that the I_D/I_G values of the wear scars for all films are higher than the I_D/I_G values of the films themselves, suggesting the graphitization of the transfer film during friction. This indicates that during high-speed friction between the ball and the film, the generated heat and the interaction forces cause the sp^3 bonds within the film to transition to sp^2 bonds. Previous work also proved that the sp^3−C atoms could only be short-lived and gradually transform into sp^2−C atoms with the graphitization generated on the wear surface of the films [38]. A graphite transfer film forms on the surface of the ball, providing lubrication during the friction process. Therefore, with an increase in friction time, the friction coefficients of the films decrease.

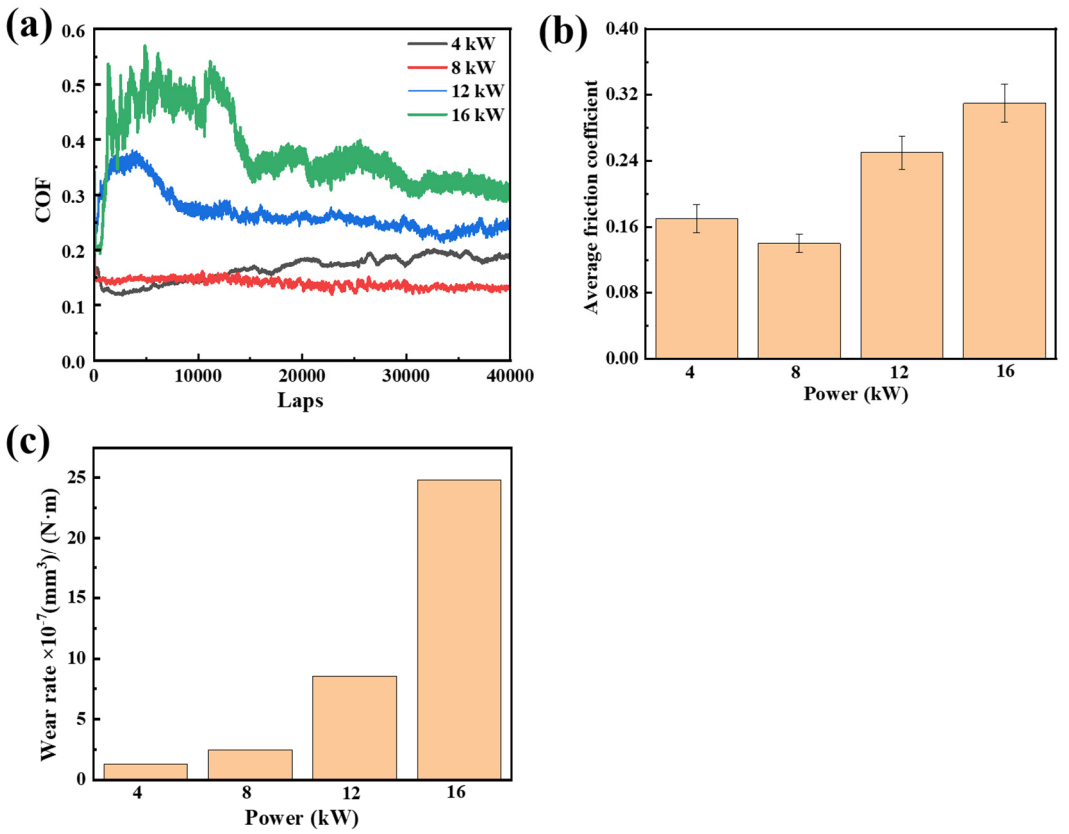

Figure 9. (**a**) Friction coefficient curves, (**b**) average friction coefficient, and (**c**) wear rates of films with various target powers.

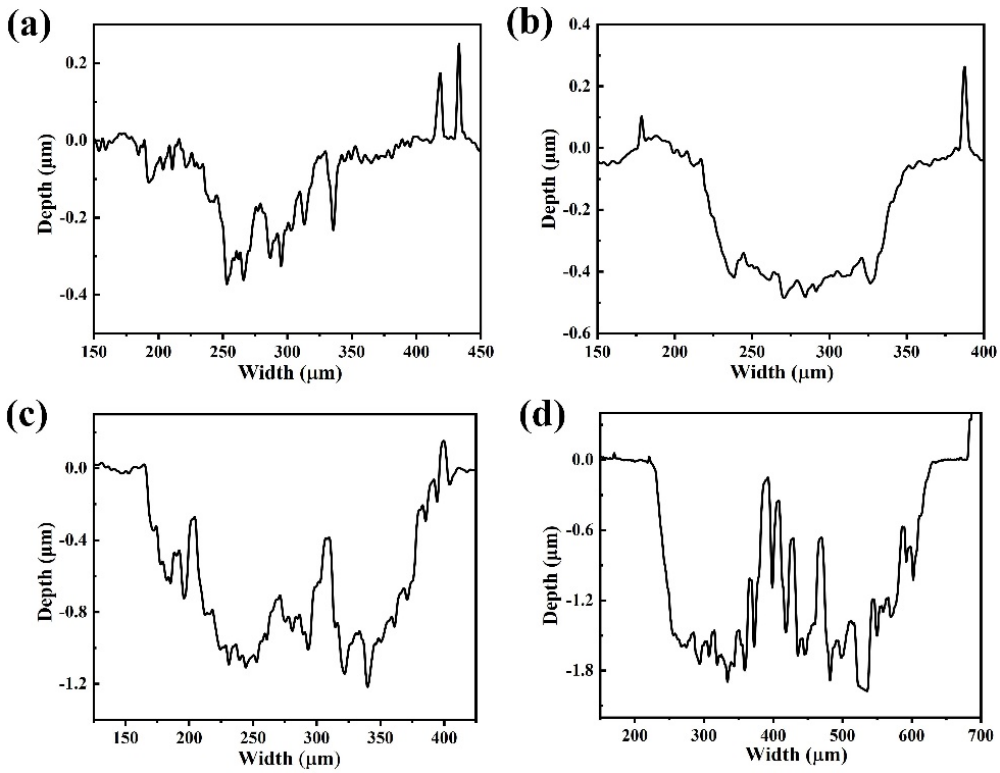

Figure 10. Wear profile curves of films with various target powers: (**a**) 4 kW, (**b**) 8 kW, (**c**) 12 kW, and (**d**) 16 kW.

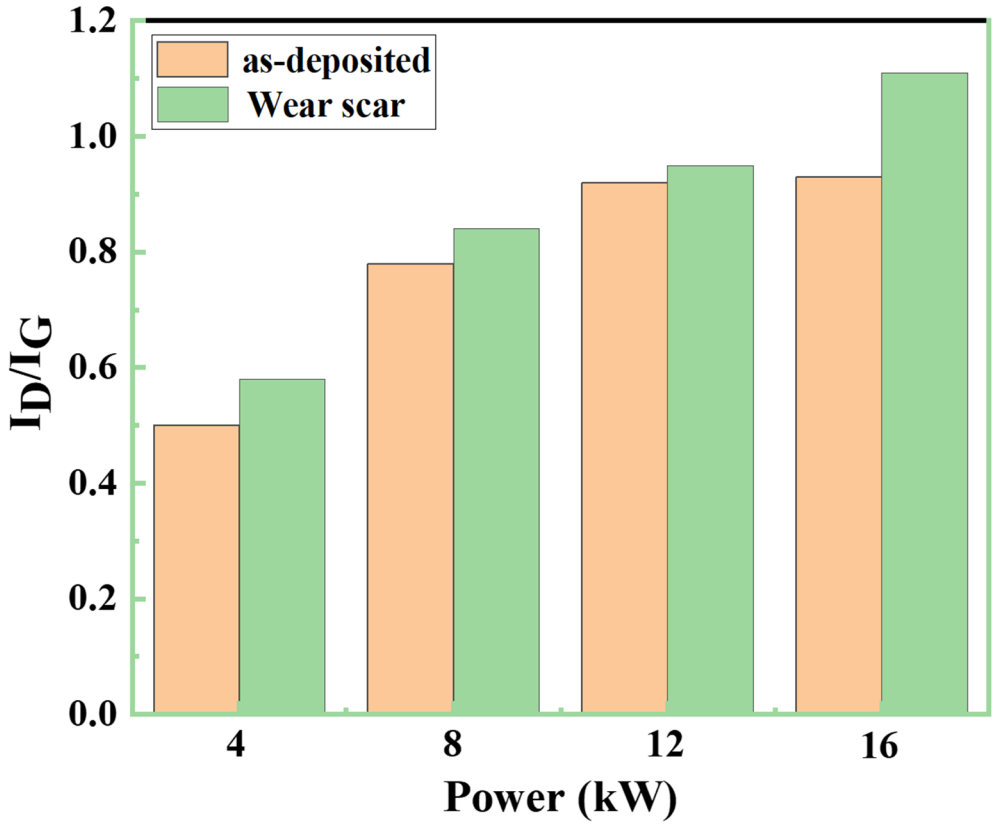

Figure 11. I_D/I_G values of films and wear scars.

4. Conclusions

In this work, to improve the comprehensive properties of titanium alloys, diamond-like carbon films with Cr doping on the surfaces of titanium alloys were deposited via high-power pulsed magnetron sputtering technology. The considerable properties of titanium alloy substrates, including mechanical and tribological properties, were achieved. The effect of target power on the microstructure and the mechanical and tribological properties of the films was studied in detail. It was found that the Cr content in films could be adjusted by varying the Cr target power, increasing from 3.73 at. % to 22.65 at. % with an increase in target power. The microstructure of the film evolved from an amorphous structure to the nanocomposite structure consisting of carbides embedded in an amorphous carbon matrix. The I_D/I_G ratios linearly increased, implying that the sp^2-C content in the film could be governed by changing the target power. The hardness of the films increased with an increase in power from 4 to 12 kW, and decreased slightly with a power of 16 kW. The formed hard carbides were responsible for the hardness enhancement. Serious abrasive wear occurred in the films deposited at a higher target power due to the excessive hard particles. The wear rates showed the same changing trend as H^3/E^2 as the target power rose from 4 kW to 16 kW. The lowest wear rate of 1.28×10^{-7} $mm^3/N{\cdot}m$ was obtained for the film deposited at 4 kW.

Author Contributions: Writing—original draft, S.L.; investigation, W.Z.; writing—review and editing and supervision, J.D.; methodology, Y.L.; formal analysis, W.Y.; conceptualization and data curation, Y.Y.; software, X.L.; formal analysis and resources, J.Y.; project administration, J.Z. All authors have read and agreed to the published version of the manuscript.

Funding: This work was financially supported by the National Natural Science Foundation of China (No. 52101063), the Natural Science Foundation of the Anhui Higher Education Institutions of China (No. 2022AH050312; KJ2021A0392), and the Open Project of China International Science and Technol-

ogy Cooperation Base on Intelligent Equipment Manufacturing in Special Service Environment (No. ISTC2023KF02).

Institutional Review Board Statement: Not applicable.

Informed Consent Statement: Not applicable.

Data Availability Statement: Data are contained within the article.

Conflicts of Interest: Author Weibo Yu was employed by the company Changzhou Huachuang Aviation Technology Co., Ltd. Author Jing Yuan was employed by the company Anhui HERO Electronic Sci & Tec Co., Ltd.

References

1. Sadeghpour, S.; Javaheri, V.; Bruschi, S.; Kömi, J.; Karjalainen, P. Strain rate and mechanical stability in determining deformation behavior of beta Ti alloys. *Mater. Sci. Eng. A* **2020**, *798*, 140274. [CrossRef]
2. Ren, L.; Xiao, W.; Kent, D.; Wan, M.; Ma, C.; Zhou, L. Simultaneously enhanced strength and ductility in a metastable β-Ti alloy by stress-induced hierarchical twin structure. *Scr. Mater.* **2020**, *184*, 6–11. [CrossRef]
3. Shao, L.; Li, W.; Li, D.; Xie, G.; Zhang, C.; Zhang, C.; Huang, J. A review on combustion behavior and mechanism of Ti alloys for advanced aero-engine. *J. Alloys Compd.* **2023**, *960*, 170584. [CrossRef]
4. Jain, S.; Parashar, V. Comparison of priori and posteriori approach of multi-objective optimization for wedm on Ti6Al4V alloy. *Mater. Res. Express* **2022**, *9*, 076504. [CrossRef]
5. Zhang, B.; Cai, Z.; Gan, X.; Zhu, M.; Yu, H. Dual motion fretting wear behaviors of titanium and its alloy in artificial saliva. *Trans. Nonferr. Met. Soc. China* **2014**, *24*, 100–107. [CrossRef]
6. Kashyap, V.; Ramkumar, P. DLC coating over pre-oxidized and textured Ti6Al4V for superior adhesion and tribo-performance of hip implant. *Surf. Coat. Technol.* **2022**, *440*, 128492. [CrossRef]
7. Ghahramanzadeh Asl, H. Investigation of friction and wear performance on oxidized Ti6Al4V alloy at different temperatures by plasma oxidation method under ambient air and vacuum conditions. *Vacuum* **2020**, *180*, 109578. [CrossRef]
8. Zhou, Z.-Y.; Liu, X.-B.; Zhuang, S.-G.; Yang, X.-H.; Wang, M.; Sun, C.-F. Preparation and high temperature tribological properties of laser in-situ synthesized self-lubricating composite coatings containing metal sulfides on Ti6Al4V alloy. *Appl. Surf. Sci.* **2019**, *481*, 209–218. [CrossRef]
9. Kümmel, D.; Schneider, J.; Gumbsch, P. Influence of interstitial oxygen on the tribology of ti6al4v. *Tribol. Lett.* **2020**, *68*, 96. [CrossRef]
10. Wang, J.; Ma, J.; Huang, W.; Wang, L.; He, H.; Liu, C. The investigation of the structures and tribological properties of f-dlc coatings deposited on Ti-6Al-4V alloys. *Surf. Coat. Technol.* **2017**, *316*, 22–29. [CrossRef]
11. Zhang, S.; Huang, T.; Sun, S.; Wu, S.; Yang, X.; Guo, F.; Zhang, B.; Dai, L. Effects of bias voltages on the tribological behaviors of DLC Coatings. *Coatings* **2024**, *14*, 176. [CrossRef]
12. Wang, J.; Wang, L.; Chen, H.; Wang, H. Molecular dynamics simulation of friction in dlc films with different sp3 contents. *Tribol. Int.* **2023**, *190*, 109050. [CrossRef]
13. Tillmann, W.; Wittig, A.; Dias, N.F.L.; Stangier, D.; Thomann, C.A.; Moldenhauer, H.; Debus, J. Silicon- and tungsten-containing hydrogen-free and hydrogenated amorphous carbon films for friction-reducing applications. *Diam. Relat. Mater.* **2022**, *123*, 108866. [CrossRef]
14. Sha, B.; Lukianov, A.N.; Dusheiko, M.G.; Lozinskii, V.B.; Klyui, A.N.; Korbutyak, D.V.; Pritchin, S.E.; Klyui Nickolai, I. Carbon-rich amorphous silicon carbide and silicon carbonitride films for silicon-based photoelectric devices and optical elements: Application from uv to mid-ir spectral range. *Opt. Mater.* **2020**, *106*, 109959. [CrossRef]
15. Li, X.; Hou, K.; Qiu, D.; Yi, P.; Lai, X. A first principles and experimental study on the influence of nitrogen doping on the performance of amorphous carbon films for proton exchange membrane fuel cells. *Carbon* **2020**, *167*, 219–229. [CrossRef]
16. Alotaibi, S.; Nama Manjunatha, K.; Paul, S. Stability of hydrogenated amorphous carbon thin films for application in electronic devices. *Diam. Relat. Mater.* **2018**, *90*, 172–180. [CrossRef]
17. Wu, J.; Wei, P.; Liu, G.; Chen, D.; Zhang, X.; Chen, T.; Liu, H. A comprehensive evaluation of DLC coating on gear bending fatigue, contact fatigue, and scuffing performance. *Wear* **2024**, *536–537*, 205177. [CrossRef]
18. Ding, J.C.; Cheng, Y.; Zhang, S.; Wang, Q.; Zhang, T.F. Microstructure, mechanical and tribological properties of ti doped ta-c films deposited by a hybrid coating system. *Diam. Relat. Mater.* **2023**, *131*, 109565. [CrossRef]
19. Ding, J.C.; Dai, W.; Zhang, T.F.; Zhao, P.; Yun, J.M.; Kim, K.H.; Wang, Q.M. Microstructure and properties of nb-doped diamond-like carbon films deposited by high power impulse magnetron sputtering. *Thin Solid Films* **2018**, *663*, 159–167. [CrossRef]
20. Guo, C.-Q.; Li, H.-Q.; Peng, Y.-L.; Dai, M.-J.; Lin, S.-S.; Shi, Q.; Wei, C.-B. Residual stress and tribological behavior of hydrogen-free al-dlc films prepared by hipims under different bias voltages. *Surf. Coat. Technol.* **2022**, *445*, 128713. [CrossRef]
21. Santiago, J.A.; Fernández-Martínez, I.; Sánchez-López, J.C.; Rojas, T.C.; Wennberg, A.; Bellido-González, V.; Molina-Aldareguia, J.M.; Monclús, M.A.; González-Arrabal, R. Tribomechanical properties of hard cr-doped dlc coatings deposited by low-frequency hipims. *Surf. Coat. Technol.* **2020**, *382*, 124899. [CrossRef]

22. Jain, V.; Roychowdhury, T.; Kuimelis, R.G.; Linford, M.R. Differences in surface reactivity in two synthetic routes between hipims and dc magnetron sputtered carbon. *Surf. Coat. Technol.* **2019**, *378*, 125003. [CrossRef]
23. Ma, D.; Harvey, T.J.; Wellman, R.G.; Ehiasarian, A.P.; Hovsepian, P.E.; Sugumaran, A.A.; Purandare, Y.P.; Wood, R.J.K. Cavitation erosion performance of cralyn/crn nanoscale multilayer coatings deposited on Ti6Al4V by hipims. *J. Alloys Compd.* **2019**, *788*, 719–728. [CrossRef]
24. Costa, A.; Ferreira, F.; Colaux, J.L.; Vahidi, A.; Serra, R.; Oliveira, J. Effect of hydrogen incorporation on the mechanical properties of dlc films deposited by hipims in doms mode. *Surf. Coat. Technol.* **2023**, *473*, 129980. [CrossRef]
25. Solomon, I.; Bhatnagar, M.; Shukla, K.; Sarma, B.; Ranjan, M.; Sarma, A. Correlation of structural and optical properties of pvd grown amorphous carbon thin films. *Diam. Relat. Mater.* **2017**, *75*, 69–77. [CrossRef]
26. Kouznetsov, V.; Macák, K.; Schneider, J.M.; Helmersson, U.; Petrov, I. A novel pulsed magnetron sputter technique utilizing very high target power densities. *Surf. Coat. Technol.* **1999**, *122*, 290–293. [CrossRef]
27. Ganesan, R.; Fernandez-Martinez, I.; Akhavan, B.; Matthews, D.T.A.; Sergachev, D.; Stueber, M.; McKenzie, D.R.; Bilek, M.M.M. Pulse length selection in bipolar hipims for high deposition rate of smooth, hard amorphous carbon films. *Surf. Coat. Technol.* **2023**, *454*, 129199. [CrossRef]
28. Brenning, N.; Hajihoseini, H.; Rudolph, M.; Raadu, M.A.; Gudmundsson, J.T.; Minea, T.M.; Lundin, D. HiPIMS optimization by using mixed high-power and low-power pulsing. *Plasma Sources Sci. Technol.* **2021**, *30*, 015015. [CrossRef]
29. Huo, C.; Lundin, D.; Raadu, M.A.; Anders, A.; Gudmundsson, J.T.; Brenning, N. On the road to self-sputtering in high power impulse magnetron sputtering: Particle balance and discharge characteristics. *Plasma Sources Sci. Technol.* **2014**, *23*, 025017. [CrossRef]
30. Fernandes, F.; Calderon, V.S.; Ferreira, P.J.; Cavaleiro, A.; Oliveira, J.C. Low peak power deposition regime in hipims: Deposition of hard and dense nanocomposite Ti-Si-n films by doms without the need of energetic bombardment. *Surf. Coat. Technol.* **2020**, *397*, 125996. [CrossRef]
31. Adelhelm, C.; Balden, M.; Rinke, M.; Stueber, M. Influence of doping (Ti, V, Zr, W) and annealing on the sp^2 carbon structure of amorphous carbon films. *J. Appl. Phys.* **2009**, *105*, 033522. [CrossRef]
32. Peng, Y.-L.; Guo, C.-Q.; Lin, S.-S.; Shi, Q.; Wei, C.-B.; Su, Y.-F.; Wu, Y.-Q.; Tang, P.; Zhu, X.-G.; Dai, M.-J. Effects of working pressure on structure and properties of al-containing amorphous carbon films prepared by high-power impulse magnetron sputtering. *J. Alloys Compd.* **2020**, *816*, 152587. [CrossRef]
33. NIST X-ray Photoelectron Spectroscopy Database (SRD 20), Version 5.0. Available online: https://srdata.nist.gov/xps/EnergyTypeElement (accessed on 25 June 2024).
34. Zhu, L.; Li, J.; Kang, J.; Tang, L.; Ma, G.; Han, C.; Shi, J.; Wang, H. Different cr contents on the microstructure and tribomechanical properties of multi-layered diamond-like carbon films prepared by unbalanced magnetron sputtering. *J. Mater. Eng. Perform.* **2020**, *29*, 7131–7140. [CrossRef]
35. Yang, L.; Chen, Y.; Xu, Z.; Toshiaki, N.; Xi, Y.; Ni, Q. Effect of heat treatment on mechanical property of amorphous carbon films by magnetron sputtering. *Diam. Relat. Mater.* **2022**, *129*, 109328. [CrossRef]
36. Tao, H.; Tsai, M.T.; Chen, H.-W.; Huang, J.C.; Duh, J.-G. Improving high-temperature tribological characteristics on nanocomposite cralsin coating by mo doping. *Surf. Coat. Technol.* **2018**, *349*, 752–756. [CrossRef]
37. Dai, W.; Ke, P.; Wang, A. Microstructure and property evolution of cr-dlc films with different Cr content deposited by a hybrid beam technique. *Vacuum* **2011**, *85*, 792–797. [CrossRef]
38. Zhou, Y.; Chen, Z.; Zhang, T.; Zhang, S.; Xing, X.; Yang, Q.; Li, D. Metastable hybridized structure transformation in amorphous carbon films during friction—A study combining experiments and MD simulation. *Friction* **2023**, *11*, 1708–1723. [CrossRef]